THE ASTROPHYSICAL JOURNAL, 225:346–356, 1978 October 15

ROCKET ULTRAVIOLET IMAGERY OF THE ANDROMEDA GALAXY

GEORGE R. CARRUTHERS,* HARRY M. HECKATHORN,† AND CHET B. OPAL*

Received 1978 January 31; accepted 1978 April 20

ABSTRACT

Far-ultraviolet (1230–2000 Å) images, with about 40″ resolution, were obtained of the Andromeda galaxy (M31) with an electrographic Schmidt camera during a sounding rocket flight 1976 October 29. The images were compromised by corona discharge in the camera and by the relatively low UV surface brightness of M31. Nevertheless, two conspicuous features are evident in the UV images: one coincident with the nucleus of the galaxy and one which corresponds to the bright stellar association NGC 206 in the SW region of the disk. These images, along with the images of 17 foreground galactic stars and laboratory calibration exposures, were microdensitometered to provide both relative and absolute flux measurements of the sources.

The UV sources in M31 are extended. In particular, the source centered on the nucleus is elongated in the direction of the major axis of the galaxy; and the UV isophotes resemble ellipses of greater eccentricity than those observed in the visible wavelength range. The observations suggest that the UV radiation in the nuclear region of M31 is due to stars lying close to the equatorial plane of the galaxy; hence these are young, early-type stars rather than highly evolved ones or a nonthermal point source.

Subject headings: galaxies: individual — galaxies: nuclei — galaxies: stellar content — ultraviolet: general

I. INTRODUCTION

Galaxies of all Hubble types were observed with the far-ultraviolet filter photometers of the University of Wisconsin from the *OAO 2* spacecraft (Code 1969; Code, Welch, and Page 1972; Code and Welch 1978). *OAO 2* observations of the Andromeda galaxy, made with a 10′ circular aperture, revealed the expected signatures of early-type star associations in the spiral arms but also revealed a peak in the far-ultraviolet emission centered on the nucleus. An additional observation of the nucleus of M31 at 1570 Å has been reported by Deharveng *et al.* (1976). As far as we know, the only other previous far-UV observations of galaxies are of the Large Magellanic Cloud and several NGC galaxies, which were imaged with an electrographic Schmidt camera (experiment S201) placed on the lunar surface during the *Apollo 16* mission (Carruthers and Page 1972; Page and Carruthers 1977).

The source of the ultraviolet radiation in the nuclear regions of galaxies has been the subject of theoretical interest since observations were first reported by Code (1969). Hills (1971) suggested that hot ($T_e \gtrsim 10^5$ K), highly evolved stars (e.g., central stars of planetary nebulae and hot white dwarfs) could account for the UV light in M31. Similarly, Rose and Tinsley (1974) have proposed that these "ultraviolet stars" may explain the UV radiation observed in the cores of some early-type galaxies. If evolved UV stars were responsible for the observed UV radiation in M31, then it would be expected that they would be distributed like the old stellar population (i.e., the shapes and orientations of UV isophotes should resemble isophotes observed at visible wavelengths).

On the other hand, Tinsley (1971, 1972) has suggested that the UV radiation may come from hot, young main-sequence stars which have recently condensed from the gas presumably generated by star deaths or general stellar mass loss in the inner disk of M31. According to the scenario of Spinrad *et al.* (1971), the central region accretes this infalling gas, forming a collapsed central disk which might be the seat of continued star formation. If this view is correct, then the newly formed stars will be confined within the disk of accreted gas near the equatorial plane of M31 and their distribution should be such that UV isophotes will resemble ellipses of greater eccentricity than those observed in visible light.

A third possibility is that the radiation is not due to stars but is nonthermal—the result of violent activity in the nucleus, such as is observed in the central region of Seyfert galaxies. If such were the case, then it would be expected that the source would be highly condensed and starlike.

In this paper, we report the first far-ultraviolet electrographic imagery of M31. The observations were obtained during a sounding rocket flight and are suitable for quantitative photometry and the derivation of spatial intensity distributions. Therefore, these observations have the potential to help define the nature, as well as the intensities, of the UV sources in the nuclear region of M31.

* E. O. Hulburt Center for Space Research, Naval Research Laboratory, Washington.

† Department of Physics, Johns Hopkins University, Baltimore.

II. OBSERVATIONS

The instrument used for the UV imagery of M31 was an electrographic Schmidt camera sensitive in the 1230–2000 Å wavelength range. This camera was similar to, but larger than, other electrographic Schmidt cameras used in the NRL rocket astronomy program and in the S201 instrument (Carruthers 1973, 1974; Carruthers and Opal 1972). It had a 15 cm effective aperture, a focal length of 30 cm (f/2), and an 11° field of view. The plate scale was 12.2 mm^{-1}. The resolution in the imagery discussed here (including the effects of the microdensitometry) was such that 50% of the energy from a point source was confined within a circle of 40″ radius. However, the limiting resolution in direct viewing of faint star images on the original negatives was considerably better (about 40″ diameter for the central brightest portion of the images).

The camera was flown on an Aerobee 200 rocket (NASA 25.056 DG) from White Sands Missile Range on 1976 October 29. The rocket attitude control system was programmed to point the camera at two targets during the flight: M31 (longest exposure, 101.6 s) and the North America Nebula, NGC 7000 (longest exposure, 50 s). The latter field partially overlapped one of the fields observed by the S201 experiment (Carruthers and Page 1976) and allowed a quantitative comparison of the camera sensitivities.

The expected sensitivity and resolution were achieved; unfortunately, however, the longer exposures (particularly of M31) were significantly degraded by corona discharge within the camera, which produced a strong background fog, highly variable with position, on the processed exposures. In the 101.6 s exposure on M31, this fogging completely obscured the northern third of the galaxy image. Two shorter-exposure (9.9 s and 40.5 s) images were also obtained: In the 40.5 s exposure on M31, the corona background was less intense but the galaxy image was nearly undetectable because of underexposure. Therefore, all the results for M31 reported here are from the 101.6 s exposure, although the two shorter exposures were useful for measurements of foreground galactic star images for comparison purposes.

Figure 1 (Plate 1) is a negative print of a portion of the 101.6 s far-UV exposure on M31 compared with a ground-based (Palomar 48 inch [1.2 m] Schmidt) blue-light photograph. It was immediately obvious, on the basis of the comparison of the present camera's sensitivity with that of the S201 instrument by way of the Cygnus imagery, that the far-UV surface brightness of M31 is far less than that of the Large Magellanic Cloud. Only two very conspicuous features are evident in the UV image of M31 in Figure 1: one which corresponds to a bright association in the southwest region of the disk (NGC 206) and one centered on the nucleus of the galaxy. There are, however, also indications of the general spiral-arm structure, although these features are underexposed and are compromised by the corona discharge fogging. Although the F star SAO 036585 is detected, the elliptical companion galaxy M32 is not. (The other companion galaxy, NGC 205, also is not detected but lies in a region of higher corona fogging.) As shown in the following, a considerable improvement in the quantitative interpretation of the imagery was possible by means of background subtraction.

III. ANALYSIS

The three flight frames of the Andromeda field were scanned with a Grant microdensitometer at NRL in the same manner as were frames from a previous flight in which the constellation Orion was observed (Carruthers and Opal 1977*a*, *b*). However, because of the larger diameter (60 mm) and higher resolution of the present frames, it was impractical to raster scan the complete images. Instead, a 250′ × 250′ area centered on the position of the nucleus of the galaxy was scanned on the two longer exposures. In addition, 24′ × 24′ areas centered on 17 foreground galactic stars with known photoelectric *UBV* magnitudes were scanned on those plates where the images were not grossly overexposed. Only seven of these stars have published MK spectral types, and six were previously observed in the UV by the Celescope experiment aboard *OAO 2*. Preflight calibration images were scanned during the same measuring session so that absolute fluxes could be derived. All scans were made using a 20 μm × 20 μm aperture and 20 μm (~15″) steps. The optical densities $d = \log_{10} I_0/I$ were recorded on magnetic tape for computer processing.

The optical densities were corrected for the nonlinear response of the recording emulsion (NTB-3) using the empirical formula $D = d' \exp(d'/s)$, where $d' = d - d_c$ is the observed density above clear emulsion (chemical fog only), D is the density for a perfectly linear emulsion, and $\exp(d'/s)$ is a correction factor for nonlinear response. The value of s is rather independent of emulsion batch (varying by at most ±10%) and has a value near $s = 10.6$, as determined from plate material scanned with the Grant microdensitometer from three previous flights. (These included preflight calibration exposures, plus star images and diffuse Lα nightglow on flight exposures of varying exposure times.) Even at the highest densities measured ($d_{max} = 2.56$ as limited by the microdensitometer), a 10% error in the value of s would result in only a 2% error in the corrected density. Furthermore, the correction for nonlinearity becomes less important at lower densities.

a) Ultraviolet Stellar Photometry

In order to provide the basis for an in-flight calibration, instrumental UV magnitudes were determined for 17 foreground field stars. These magnitudes were then compared to those predicted by theory using the grid of line-blanketed model atmospheres computed by Kurucz, Peytremann, and Avrett (1974, hereafter KPA). This provided a check on our data reduction procedures and on the wavelength sensitivity function of the camera (Fig. 2), which was determined 2 weeks prior to launch.

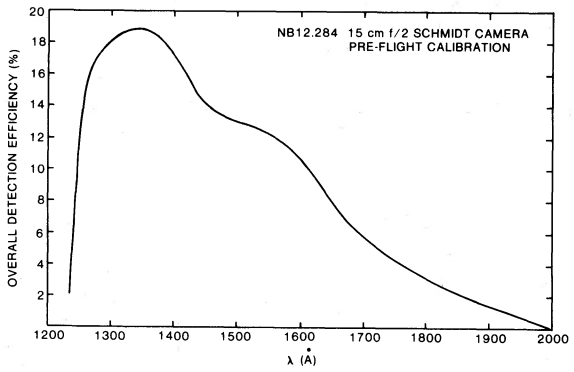

FIG. 2.—Spectral response of the flight instrument as measured 2 weeks prior to launch.

The linearized density arrays $D(x_i, y_j)$ of stellar images were corrected for plate background (with contributions from corona discharge and sky background) by subtracting a surface fitted by least squares to the densities in the area scanned (but outside of a circle of radius 4'.7 centered on the image of the star in question). General polynomial surfaces with six coefficients were used because of the variable nature of the background. The density arrays above plate background were thus expressed as

$$D'(x_i, y_j) = D(x_i, y_j) - (a_0 + a_1 x_i + a_2 y_j + a_3 x_i y_j + a_4 y_j^2 + a_5 x_i^2) .$$

The density volumes

$$D_R = \int_0^{2\pi} \int_0^{R_{\rm lim}} D'(R, \theta) R dR d\theta$$

were then computed for the stars by numerically integrating the corrected density arrays in the manner described by Jones *et al.* (1967). An empirically determined correction (based on the average density distribution of moderately exposed stellar images) was applied to D_R for the brighter stars to account for saturation of the microdensitometer.

Instrumental UV magnitudes $m_{\rm UV}^{\rm obs}$, referred to the 9.9 s exposure, were obtained by applying the precisely known ratio of exposure times to the corrected density volumes (D_R') according to the formula $m_{\rm UV}^{\rm obs} = -2.5 \log_{10} \langle D_R'(9.9/t) \rangle$. The instrumental UV magnitudes of the foreground galactic stars together with pertinent identification, spectral, and photometric data extracted from the literature are collected in Table 1.

A theoretical ultraviolet magnitude $m_{\rm UV}^{\rm calc}$ was determined for each star listed in Table 1 by convolving the wavelength sensitivity function of the flight instrument with the main-sequence ($\log g = 4.0$, solar abundance) KPA model of appropriate effective temperature (T_e). Since MK spectral types were not available for all stars observed, T_e had to be estimated solely on the basis of existing *UBV* colors, which may be affected by interstellar reddening. A plot of $U - B$ versus $B - V$ (Fig. 3) shows the stars to be only slightly reddened at visual wavelengths (the galactic latitude of M31 is $b^{\rm II} = -21°.6$). However, interstellar extinction is considerably greater in the UV. The "average" UV extinction curve of Bless and Savage (1972) shows that an ultraviolet color excess of $E(\rm UV - V) \approx 4.4\, E(B - V)$ should be expected. Therefore, the effect of interstellar reddening should be taken into consideration when comparing theory with observation, but we lack the necessary ground-based data for many of the observed field stars. Hence we assumed that all of the observed stars are unreddened [i.e., $B - V = (B - V)_0$] and assigned an effective temperature to each star using the empirical relation between T_e and $(B - V)_0$ determined by Code *et al.* (1976). We investigate later, in a qualitative manner, the effect which interstellar reddening may have in our comparison. The magnitude zero point was fixed by requiring $M_{\rm UV} - M_V \equiv 0$ for an unreddened star with $T_e = 9400$ K, $\log g = 3.9$. The theoretical ultraviolet magnitudes so calculated are given in Table 1 and are plotted versus the observed instrumental ultraviolet magnitude in Figure 4.

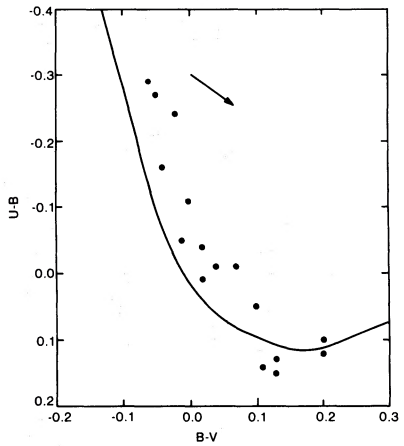

FIG. 3.—Two-color ($B - V$ versus $U - B$) diagram for stars listed in Table 1. The plotted main sequence is that adopted by Deutschman, Davis, and Schild (1976). The arrow is a linear reddening trajectory of slope $E(U - B)/E(B - V) = 0.72$; $\langle E(B - V) \rangle \approx 0.07$ using the plotted main sequence, and $\langle E(B - V) \rangle \approx 0.05$ if Johnson's (1965, 1968) main sequence is used.

The line drawn through the points in Figure 4 is the result of a least-squares fit (we rejected SAO 36702 because of its comparatively large residual and A0p spectral type) and has the form $m_{\rm UV}^{\rm calc} = 12.78 + 1.118 m_{\rm UV}^{\rm obs}$. Half of the points lie within ± 0.18 mag of the line, which departs only slightly from 45°. The slope is highly dependent on the two stars which are the faintest in the UV (SAO 53946 and 54011). These stars also have the reddest $B - V$ color indices. This suggests that our procedure for calculating the instrumental UV magnitude tends to underestimate the brightness of the faintest stars and/or the actual sensitivity of the flight instrument is not as high at longer wavelengths as implied in Figure 2. In fact, any

TABLE 1

PHOTOMETRIC AND SPECTROSCOPIC DATA FOR STARS OBSERVED IN THE ULTRAVIOLET

SAO (1)	HD (2)	BD (3)	Spect. (4)	V (5)	$B-V$ (6)	$U-B$ (7)	Hβ (8)	U2 (9)	U3 (10)	m_{UV}^{obs} (11)	N (12)	m_{UV}^{calc} (13)	S (14)	P (15)
53801	1403	+37°40	B9.5 V	9.05	0.00	−0.11	...	...	...	−3.46	3	8.94	B	B
36390	2421	+43°92	A2	5.18	+0.04	−0.01	...	...	...	−6.61	1	5.47	H	B
53946	2676	+35°83	A4 V	9.17	+0.20	+0.10	...	...	...	−0.80	2	12.08	B	B
53976	2933	+35°90	B9 V	7.94	−0.02	−0.24	...	...	...	−5.08	1	7.61	B	B
54005	3203	+34°79	A2 V	7.71	+0.07	−0.01	...	...	...	−4.15	2	8.34	B	B
54006	3202	+35°98	A0	8.56	+0.10	+0.05	...	...	...	−2.62	2	9.58	H	B
54011	3225	+35°99	A5	8.91	+0.20	+0.12	...	...	...	−0.92	2	11.82	H	B
36517	3431	+39°138	A0	6.86	+0.02	+0.01	2.882	10.24	11.50	−5.06	1	6.94	H	D
54085	3892	+38°94	B8	7.67	−0.06	−0.29	2.766	10.00	11.02	−5.53	1	6.83	H	D
36640	4335	+44°160	B8	6.02	−0.05	−0.27	...	8.61	9.16	−6.69	1	5.42	H	B
36702	4778	+44°176	A0p	6.14	+0.02	−0.04	...	9.51	11.33	−5.08	1	6.22	B	B
36718	4902	+40°177	A0	7.29	−0.04	−0.16	2.810	9.56	...	−5.46	1	6.77	H	D
54281	5448	+37°175	A5 V	3.86	+0.13	+0.15	...	...	...	−6.46	1	5.32	B	B
36833	5789 AB	+43°193	B9 V	5.70	−0.01	−0.05	...	8.88	9.45	−6.67	1	5.48	D	D
54339	5854	+37°190	A0	7.19	+0.13	+0.13	...	...	...	−3.64	2	8.65	H	B
36874	6116	+40°209	A7 V	5.93	+0.16	...	...	...	...	−4.01	1	7.97	B	B
36950	6658	+43°234	A2	5.04	+0.11	+0.14	...	...	...	−5.38	1	6.20	H	B

NOTES.—Cols. (1)–(3), star number in *Smithsonian Astrophysical Observatory* (SAO) *Star Catalog*, *Henry Draper* (HD) *Catalogue*, and *Bonner Durchmusterung* (BD). Col. (4), MK or HD spectral classification from source listed in col. (14). Cols. (5)–(7), *UBV* photometric data from source listed in col. (15). Col. (8), β index (Deutschman *et al.* 1976). Cols. (9)–(10), U2 and U3 UV magnitudes from the *Celescope Catalog of Ultraviolet Stellar Observations* (Davis *et al.* 1973). Col. (11), instrumental UV magnitude (this study). Col. (12), number of images measured to derive UV magnitude. Col. (13), UV magnitude calculated from theory (see text). Cols. (14)–(15), sources for spectral (S) and *UBV* photometric (P) data: B = Blanco *et al.* 1970, H = HD catalog, D = Deutschman *et al.* 1976.

HD 5789 AB is a visual double star (separation 7″.8) comprised of SAO 36832 and SAO 36833 which is unresolved in the electrographic image. Magnitudes and spectral classification refer to the combined light of the system.

deterioration of the photocathode during the time interval between calibration and launch would shift the effective wavelength of the instrument toward shorter wavelengths. All things considered, the agreement with expectations is reasonable.

In order to assess the effect of neglecting interstellar reddening in the comparison, the "Q-method" of Johnson and Morgan (1953) and Johnson (1958) was used to estimate the intrinsic color index $(B-V)_0$ and color excess $E(B-V)$. As before, T_e was assigned using $(B-V)_0$ and the empirical relation of Code *et al.* (1976). Unfortunately, at the effective

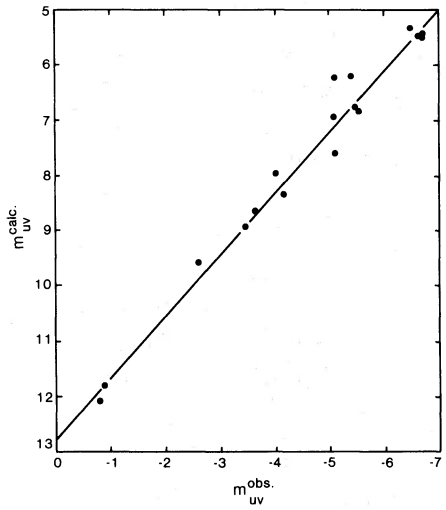

FIG. 4.—Observed instrumental UV magnitude versus the UV magnitude calculated from theoretical line-blanketed model atmospheres of main-sequence stars of solar abundance (see text). T_e was assigned solely on the basis of available *UBV* photometry, and it was assumed that $E(B-V)=0$.

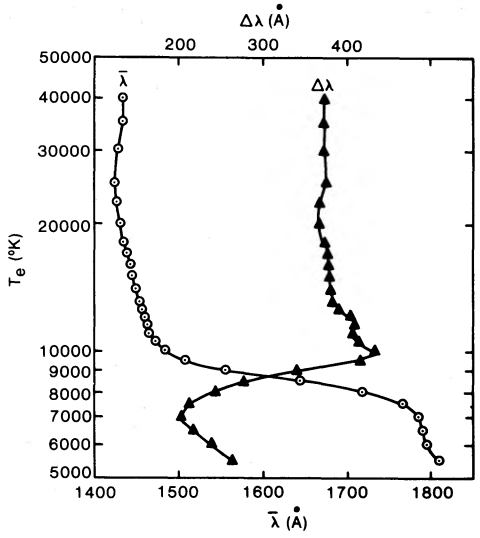

FIG. 5.—The effective wavelength ($\bar{\lambda}$) and effective bandpass ($\Delta\lambda$) of the flight instrument as a function of T_e. The relations were computed with the method described by Mathews and Sandage (1963) using the spectral response of the flight instrument and the line-blanketed model atmospheres for $\log g = 4.0$ stars of solar abundance of KPA. The relations plotted are for $E(B-V)=0$.

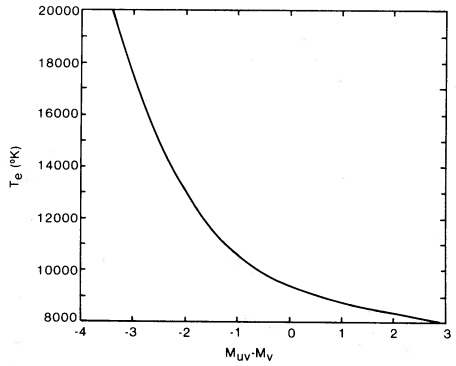

FIG. 6.—Theoretical difference in UV and V magnitudes as a function of T_e derived from the line-blanketed model atmospheres of KPA. The relation was computed for main-sequence ($\log g = 4.0$, solar abundance) stars using the spectral response of the flight instrument, and the magnitude zero point was fixed such that $M_{UV} - M_V \equiv 0$ for an unreddened star with $T_e = 9400$ K and $\log g = 3.9$. For stars cooler than late B, a small error in the assigned T_e results in a large difference in the expected UV magnitude.

wavelength of the observations (see Fig. 5), the quantity $M_{UV} - M_V$ calculated from the models is very sensitive to a small change in the adopted T_e (see Fig. 6) for late-B– and early-A–type stars. Actually, neglecting interstellar reddening in assigning effective temperatures has a greater effect on our comparison than does reddening itself at UV wavelengths. For example, if $E(B - V) = 0.05$ for a star with $T_e = 9500$ K were ignored, a temperature of 9100 K would have been assigned. This results in a change of ~ 0.5 mag in the quantity $M_{UV} - M_V$. Nevertheless, the scatter in Figure 4 was decreased when the effects of reddening were considered in the manner described. This suggests that allowance for reddening would prove beneficial in our comparison. However, it is clear that further ground-based observations of the foreground stars are necessary in order to properly compare the UV magnitudes predicted by theory with those observed in this study. Under the circumstances, the agreement as depicted in Figure 4 is quite reasonable.

b) Ultraviolet Photometry of the Nucleus of M31 and NGC 206

A different procedure was adopted in calculating the UV magnitudes of the two brightest discrete sources in M31 because they were more diffuse than the field star images and because spiral-arm features and dust lanes (faintly detected on the frames) made a polynomial surface fit of the background seem somewhat artificial. Instead, following Jones *et al.* (1967), we computed D_R (the integral of the flux density) for a number of concentric circles C_{R_j} of radius R_j, $j = 1, 2, \ldots, J$ according to

$$D_R = \int_0^{2\pi} \int_0^R D(R, \theta) R dR d\theta ,$$

where $D(R, \theta)$ represents the linearized density array $D(x_i, y_j)$ measured on the 101.6 s exposure *uncorrected for background effects*. If $A_j = \pi(R_j^2 - R_{j-1}^2)$ denotes the area between concentric circles C_{R_j} and $C_{R_{j-1}}$, then the mean density $\langle d_j \rangle$ at the effective radius $\langle R_j \rangle = (R_j + R_{j-1})/2$ is given by $\langle d_j \rangle = (D_{R_j} - D_{R_{j-1}})/A_j$. The quantity $\langle d \rangle$ (with 1 pixel $\approx$ 15″ × 15″ the unit of area) is plotted versus the effective radius $\langle R \rangle$ for the nucleus of M31 and NGC 206 in Figures 7 and 8. The "error bars" denote the quantity $\pm\{\sum [D(R, \theta) - \langle d_j \rangle]^2/(A_j - 1)\}^{1/2}$ (with the summation carried out for all pixels within the area

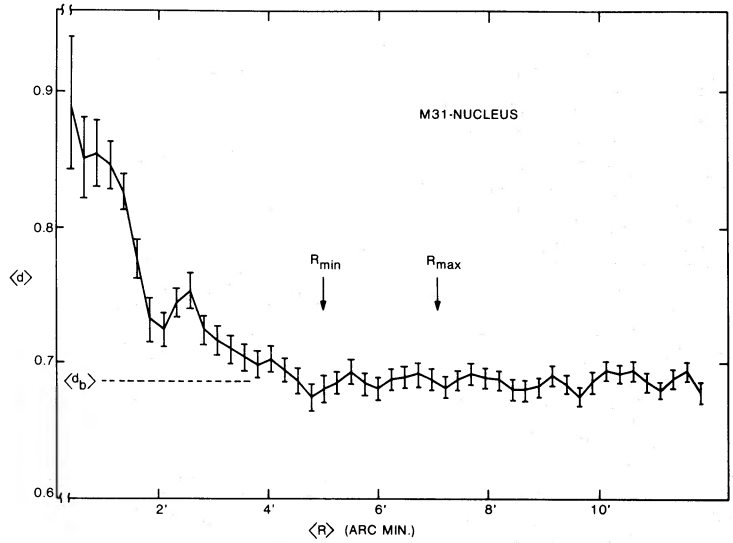

FIG. 7.—The mean density profile of the inner region of M31. The quantity $\langle d \rangle$ is the average optical density (corrected for emulsion nonlinearity) at the effective radius $\langle R \rangle$ of an annular region of thickness $\sim 15''$ centered on the position of the nucleus. The symmetrized profile appears to merge with the background at radii greater than $R_{lim} = R_{min} = 5'$.

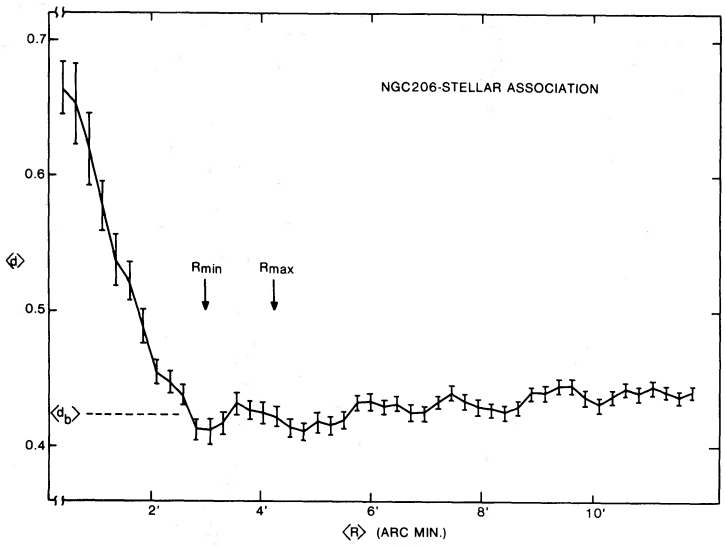

FIG. 8.—The mean density profile of the stellar association NGC 206. The profile of the association appears to merge with the background at radii greater than $R_{\rm lim} = R_{\rm min} = 3'$. The positive slope of the background at radii greater than $\sim 5'$ is due to corona and apparent spiral-arm structure west and south of the image of the association.

A_j) and give a feeling of the degree of variability of the background within each annular region. The nucleus of M31 merges into the background (artificially made radially symmetric by this procedure) at $R_{\rm lim} \gtrsim 5'$, while NGC 206 appears to be somewhat more compact and is lost in the background at $R_{\rm lim} \gtrsim 3'$. The plate background was assumed to be constant within these radii and was represented by the mean density of an annular region centered on the object whose inner radius corresponded to $R_{\rm lim}$. For the nucleus of M31, the annular region was defined by $R_{\rm min} = 5'$ and $R_{\rm max} = 7'.07$ such that its area equaled the area inside the circle of radius $R_{\rm lim}$. The mean density in this annular region $\langle d_b \rangle = 0.687$. Similarly, for NGC 206, $R_{\rm min} = 3'$, $R_{\rm max} = 4'.24$, and $\langle d_b \rangle = 0.424$. No correction for microdensitometer saturation is necessary, since the peak densities are well below $d_{\rm max}$. Density volumes, corrected for background, were then computed according to

$$D_R' = \int_0^{2\pi} \int_0^R [D(R, \theta) - \langle d_b \rangle] R dR d\theta .$$

A plot of D_R' versus R is given in Figure 9 for the two extragalactic objects. The average density distribution of three moderately exposed stars (as determined by the methods of § III*a*) is shown for comparison. For the nucleus of M31 at $R_{\rm lim} = 5'$, we adopt a density volume $D_R' = 44.55$; for NGC 206, where $R_{\rm lim} = 3'$, we adopt $D_R' = 29.73$. Applying the ratio of exposure times (9.9 s/101.6 s), we derive $m_{\rm UV}^{\rm obs} = -1.59$ for the nucleus of M31 and $m_{\rm UV}^{\rm obs} = -1.15$ for NGC 206. These magnitudes should be considered as representative of the nucleus and association alone, since any luminosity due to underlying spiral structure would, in principle, have been removed when the background was subtracted.

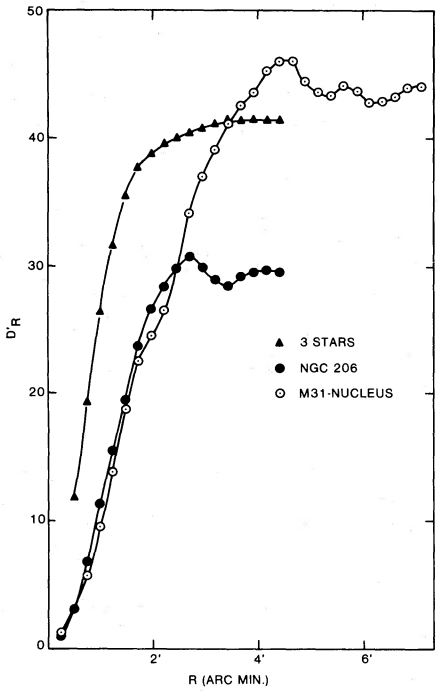

FIG. 9.—The integrated luminosity distributions D_R' of the nuclear region of M31 and NGC 206. Constant background densities of $\langle d_b \rangle = 0.687$ and 0.424 were assumed for the nucleus and association, respectively. The integrals were taken over circular regions of radius R centered on the objects. The average integrated luminosity distribution for three stars is plotted for comparison.

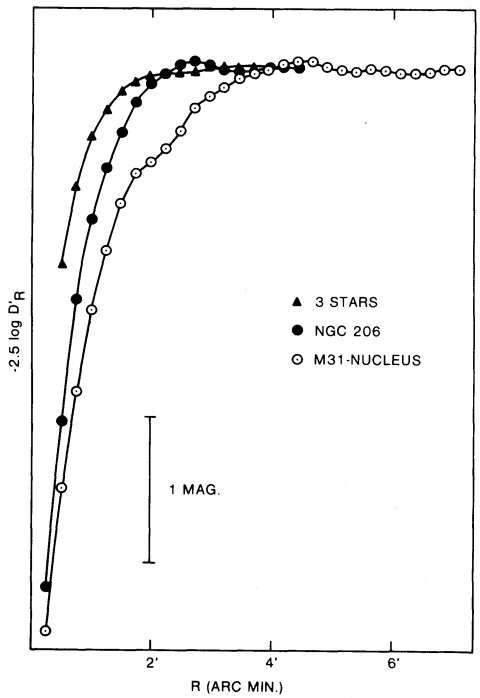

FIG. 10.—The integrated luminosity distributions of Fig. 9 expressed in magnitude units. The positions of the curves have been adjusted vertically so that they coincide at $R > R_{\rm llm}$ to show the extended nature of the extragalactic objects.

In order to demonstrate the extended nature of the extragalactic sources, Figure 10 presents the data of Figure 9 expressed in magnitude units. The curves have been shifted vertically to coincide at $R > R_{\rm llm}$. It is clear from the shapes of these curves that the extragalactic objects are not point sources. For the stars, 50% of the luminosity is confined within a circle of radius 0.'7. For the nucleus and association, the radii are 1.'7 and 1.'2, respectively.

Figure 11 presents two reconstructions of the M31 imagery. Areas judged free of foreground stars, the two prominent sources in M31, and areas weakly showing spiral-arm structure were fitted with a general polynomial surface with 10 coefficients. This "best-effort" background determination was then subtracted from the linearized density array, and the resulting array is presented in the form of an isodensity contour plot (left side of Fig. 11), where the densities above background are roughly proportional to UV brightness. On the right is a pseudophotographic reproduction with shading proportional to density above background. Comparison with Figure 1 shows considerable qualitative improvement, although two areas (to the upper left, and in a near-vertical stripe to the right, of each plot) still contain corona discharge contributions. The detectability of faint features is not increased, however, in part because of the "smoothing" of discrete features introduced by the microdensitometry and computer processing, and in part because the background subtraction may in some cases remove some real signal as well.

The absolute far-UV brightnesses of the two primary sources in M31 may be determined in two ways: (*a*) by comparison of their density volumes with those of preflight calibration images, or (*b*) by comparison of their density volumes (or UV magnitudes) with those of foreground field stars whose far-UV brightnesses have been determined theoretically (or, in the best case, by previous far-UV measurements).

We first derive the absolute far-UV brightness of the central source in M31 using our preflight calibration. The calibration image chosen for the comparison was of a diffuse source ($\sim$10.'5 in diameter) of nearly monochromatic radiation (O I 1304 Å emission, produced by a microwave discharge lamp running on an O_2–He mixture). The peak (and nearly constant) density of this image was 0.90; therefore, there is minimal contribution to the calibration uncertainty due to effects of emulsion nonlinearity, camera resolution, or photoelectron statistics. The total density volume (D_R') of this image was 1318, and the monitor photomultipliers indicated a 1304 Å photon flux of 9065 photons $cm^{-2}\,s^{-1}$ during the 10 s exposure. The derived absolute sensitivity, combined with the spectral response folded with the 10,000 K KPA model, yields a far-UV flux from the M31 nuclear source of 0.078 photons $cm^{-2}\,s^{-1}\,Å^{-1}$ at 1550 Å. This is a factor of about 1.5 brighter than the measurement of Code and Welch (1978), who derived a flux $F(1550\ Å) = 6.9 \times 10^{-13}$ ergs $cm^{-2}\,s^{-1}\,Å^{-1}$ (0.054 photons $cm^{-2}\,s^{-1}\,Å^{-1}$) for the 10′ diameter region centered on the nucleus. We consider this to be satisfactory agreement, particularly since the *OAO 2* measurement includes not only the nucleus but other stars and inner spiral-arm structure within its 10′ diameter field.

We now consider, as a check on the preflight calibration, the use of field star images for in-flight calibration. To minimize uncertainties introduced by the convolution of the camera response curve and the KPA model fluxes, we use the earliest comparison star for which we have adequate measurements on our plates, in this case SAO 53801 (B9.5 V, $V = 9.05$). The UV magnitudes of the M31 nucleus and NGC 206 are fainter by 1.87 and 2.31 mag, respectively, assuming the 10,000 K (B9.5 V) model of KPA to apply to all three objects. The measurement of Code and Welch (1978) of the nuclear region of M31 is equivalent to the flux of a KPA 10,000 K star with $V = 10.2$, or 0.72 mag *brighter* than our measurement. Since correction for any reddening of the comparison star SAO 53801 will increase our brightness determination of the M31 nucleus [a reddening of $E(B - V) = 0.05$ translates to $E(1550\ Å - V) = 0.22$ mag], the deficiency relative to *OAO 2* is reduced to about 0.5 mag, or a factor of 1.5, in the opposite sense from the factor of 1.5 disagreement based on the preflight calibration.

In summary, therefore, our measurement of the far-UV brightness of the M31 nuclear region agrees to $\pm$50% with the *OAO 2* determination but does not support the much higher value reported by Deharveng *et al.* (1976).

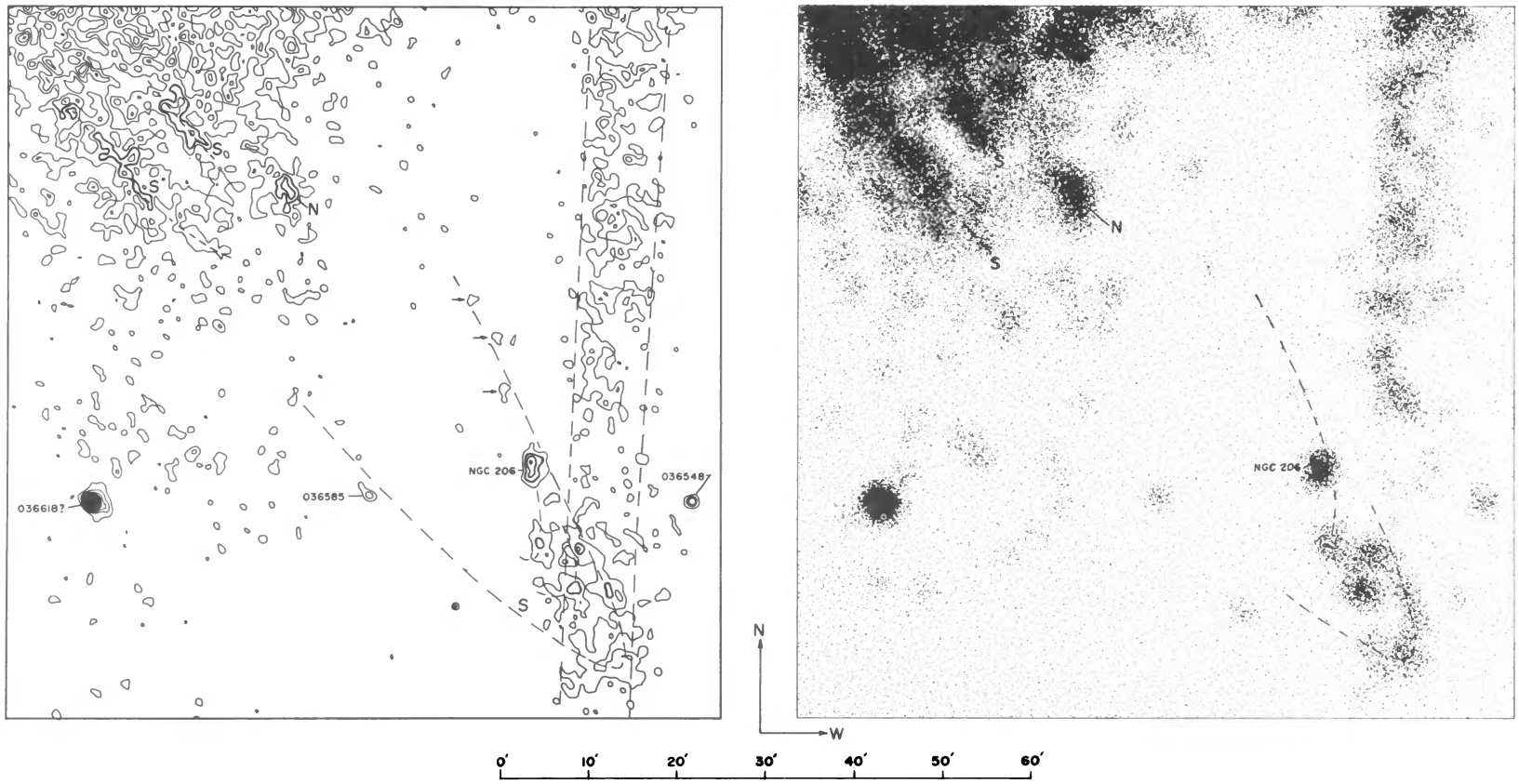

FIG. 11.—Two reconstructions of the M31 imagery after subtraction of a general polynomial surface with 10 coefficients (our "best-effort" background determination). In the isodensity contour plot (*left*), the minimum contour level is $D_{\min} = 0.075$ density units above the background and the contour interval is $\Delta D = 0.075$. In the pseudophotographic representation (*right*), the degree of shading is proportional to density above background. The positions of foreground stars, the two sources in M31, and spiral-arm features (faintly visible) are indicated. While the effects of corona background are not completely removed in our reconstructions, as is apparent in the upper left and between the two parallel dashed lines, a comparison with Fig. 1 shows considerable qualitative improvement.

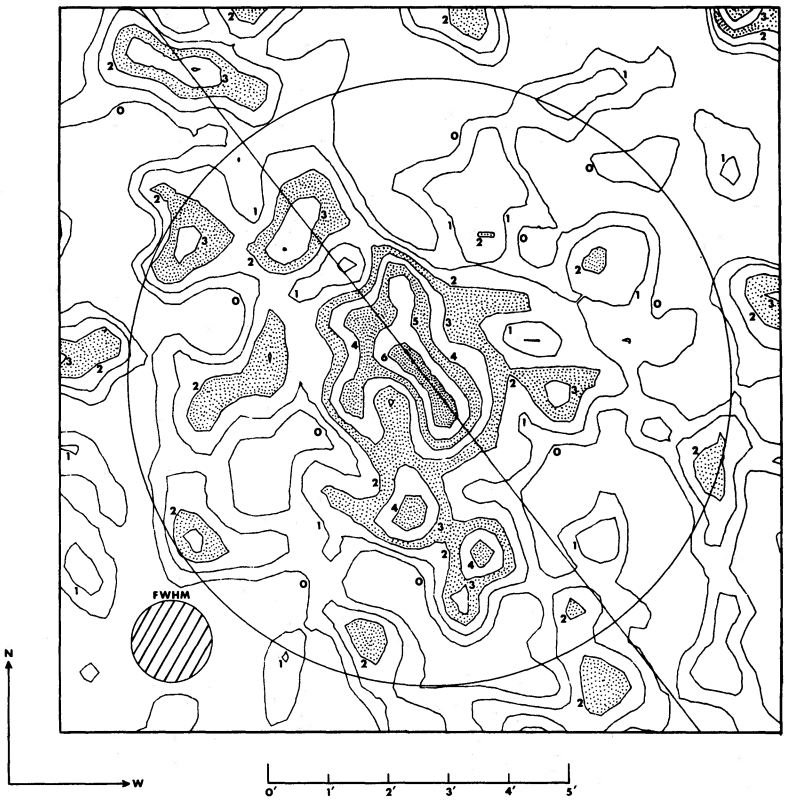

FIG. 12.—UV isophotes of the nuclear region of M31 generated from the linearized density array (smoothed as described in the text). The lowest contour (labeled 0) was set at the level of the plate background ($\langle d_b \rangle = 0.687$ density units), and the interval between successively higher contours $\Delta D = 0.04$ density units. The diagonal line is the position angle of the major axis of the galaxy, and the circle represents the 10′ aperture through which *OAO 2* is observed. The crosshatched circle represents the resolution (~40″ radius) of the present imagery after microdensitometry and computer processing.

Is the absolute far-UV brightness so derived consistent with a stellar origin for the UV flux? If we assume an absolute visual magnitude of +0.8 (Underhill 1966) for a B9.5 V star, SAO 53801 is at a distance modulus of 8.25 mag (440 pc). Hence the nucleus of M31 is equivalent in UV brightness to 4.4×10^5 such stars, and the association NGC 206 to 2.9×10^5 such stars. However, it is likely that much of the UV flux from the M31 sources is contributed by stars much hotter than 10,000 K. For example, a 30,000 K star has about 10 times the ratio N(1550 Å)/N(5500 Å) as does a 10,000 K star, and, assuming $M_V = -4.4$ (type B0 V), it has nearly 1200 times the flux at 1550 Å. Thus the M31 sources are equivalent to 370 and 240 B0 V stars, respectively. It is obvious, however, that the sources, if they are of stellar origin, are most likely a mixture of hot stars of a wide range of effective temperatures and luminosities with an effective average between these two extremes.

The angular resolution of our imagery is sufficient for us to make some definite suggestions as to the nature of the UV source in the nuclear region of M31, although the results are not completely conclusive. Figure 12 shows the UV isophotes of the nuclear region derived from the 101.6 s exposure electrograph. A constant plate background $\langle d_b \rangle = 0.687$ was subtracted from the linearized density array, which was smoothed in x and y directions using the scheme

$$D_s(x_i, y_j) = 0.25D(x_i, y_{j-1}) + 0.5D(x_i, y_j) + 0.25D(x_i, y_{j+1}) .$$

The contour interval $\Delta D = 0.04$ density units. The diagonal line is the position angle of the major axis of M31 (P.A. = 37°.7, according to de Vaucouleurs 1958) and is drawn through the brightest region of our UV imagery—a region coincident with the nucleus of the galaxy. Even with our limited resolution, it is clear that the UV image of the nucleus is extended (as shown previously in Fig. 10) and elongated in the direction of the major axis of the galaxy. This observation argues against a single, nonthermal point source for the UV radiation and in favor of an explanation invoking young, hot stars; the possibility that the source may be old, highly evolved hot stars requires further investigation.

De Vaucouleurs (1958, his Table 4 and his Fig. 6) has shown that, in blue light, the isophotes (assumed to be elliptical) in the inner regions of M31 become more and more circular as the semistellar nucleus is

TABLE 2

ADOPTED PARAMETERS: BLUE-LIGHT ISOPHOTES

a (arcmin)	b/a	Area (arcmin^2)
0.6.....	0.84	0.832
1.0.....	0.80	2.51
1.6.....	0.76	6.15
2.4.....	0.75	13.5
2.9.....	0.72	19.2
3.5.....	0.68	26.4
4.2.....	0.67	36.9

approached; i.e., the ratio of semiminor to semimajor axes $b/a \rightarrow 1.0$ as $a \rightarrow 0$. A portion of his table is reproduced in Table 2.

In order to see whether this pattern of behavior is repeated in the UV, a general two-dimensional Gaussian function

$$F(x, y) = A \exp\left\{\frac{1}{2(1-\rho^2)}\left[\left(\frac{x-x_0}{\sigma_x}\right)^2 - 2\rho\left(\frac{x-x_0}{\sigma_x}\right)\left(\frac{y-y_0}{\sigma_y}\right) + \left(\frac{y-y_0}{\sigma_y}\right)^2\right]\right\} - \langle d_b \rangle$$

was fitted by least squares (see Chiu 1977) to the linearized density array centered on the nucleus. For reasonable values of the coefficients, the intersections of planes of constant density with the Gaussian surface are ellipses. The function was fitted to the *unsmoothed* density array within a 5.'6 × 5.'6 area centered on the nucleus of M31 with all points given equal weight. Of the UV energy observed in the central region of M31 by the present experiment, 85% is confined within this area (31.4 arcmin^2 ≈ 22 resolution elements, where a resolution element is taken to be 40″ in radius). The fit was such that $b/a = 0.75$ with $a = 3.'65$ for area $A = \pi ab = 31.4$ arcmin^2. The position angle of the ellipse P.A. = 22°. If a smaller region is fitted (2.'7 × 2.'7 ≈ 7.3 arcmin^2 ≈ 5.2 resolution elements) within which ~45% of the UV energy is emitted, $b/a = 0.63$ with $a = 1.'9$ for area $A = \pi ab = 7.3$ arcmin^2 with P.A. = 31°. Hence, in contrast to the behavior in the visible spectral region, the UV isophotes tend to become more eccentric as the nucleus is approached.

Because of the small number of resolution elements involved, it would not be prudent at this time to make a firm conclusion as to the source of the UV radiation. However, the data suggest that the UV radiation in the central region of M31 is due to stars lying close to the equatorial plane of the galaxy, hence young, early-type stars rather than highly evolved ones or a nonthermal point source. Clearly, observations of higher angular resolution than those obtained in the present study are necessary before a final conclusion can be reached.

IV. CONCLUSIONS

The far-UV (1230–2000 Å) electrographic images of the Andromeda galaxy discussed here have allowed, for the first time, both absolute photometry and brightness distributions (with 40″ resolution) to be obtained for the observed features. The far-UV brightness of the central region of M31 has been confirmed to be within ±50% of that determined by Code and Welch (1978), which is $F(1550\ \text{Å}) = 0.69 \times 10^{-13}$ ergs cm^{-2} s^{-1} Å^{-1} [i.e., $N(1550\ \text{Å}) = 0.054$ photons cm^{-2} s^{-1} Å^{-1}]. The far-UV brightness of the association NGC 206 is less than that of the nuclear region by a factor of 0.67.

Both the M31 central region and NGC 206 are definitely shown to be diffuse sources, with effective radii of 1.'7 and 1.'2, respectively, at their half-intensity boundaries. The brightness distribution of the central region of M31 is a flat ellipse with its major axis in close alignment with the major axis of the galaxy. This favors a source model consisting of early-type stars close to the galactic plane, rather than a halo-type distribution of evolved, hot subdwarf stars, and is strong evidence against a nonthermal point source at the galactic center.

We thank D. King, H. Merchant, and many others for their contributions to the success of the rocket flight, which was supported by NASA. We also thank M. VanHoosier for consultations on the microdensitometry and A. Code for providing *OAO 2* measurements of M31 prior to publication. D. Yentis provided a fast, multiparameter fitting program.

REFERENCES

Blanco, V. M., Demers, S., Douglass, G. G., and FitzGerald, M. P. 1970, *Pub. U.S. Naval Obs.*, Ser. 2, Vol. **21** (B).
Bless, R. C., and Savage, B. D. 1972, in *Scientific Results from the Orbiting Astronomical Observatory* (*OAO-2*), ed. A. D. Code (NASA SP-310), p. 175.
Carruthers, G. R. 1973, *Appl. Optics*, **12**, 2501.
———. 1974, in *Electrography and Astronomical Applications*, ed. G. L. Chincarini, P. J. Griboval, and H. J. Smith (Austin: University of Texas Press), p. 93.
Carruthers, G. R., and Opal, C. B. 1972, *Proc. Soc. Photo-Opt. Instrum. Eng.*, **28**, 203.
———. 1977*a*, *Ap. J.* (*Letters*), **212**, L27.
Carruthers, G. R., and Opal, C. B. 1977*b*, *Ap. J.*, **217**, 95.
Carruthers, G. R., and Page, T. L. 1972, in *Apollo 16 Preliminary Science Report* (NASA SP-315), p. 13-1.
———. 1976, *Ap. J.*, **205**, 397.
Chiu, L.-T. G. 1977, *A.J.*, **82**, 842.
Code, A. D. 1969, *Pub. A.S.P.*, **81**, 475.
Code, A. D., Davis, J., Bless, R. C., and Hanbury Brown, R. 1976, *Ap. J.*, **203**, 417.
Code, A. D., and Welch, G. A. 1978, in preparation.
Code, A. D., Welch, G. A., and Page, T. L. 1972, in *Scientific Results from the Orbiting Astronomical Observatory* (*OAO-2*), ed. A. D. Code (NASA SP-310), p. 559.

Davis, R. J., Deutschman, W. A., and Haramundanis, K. L. 1973, *Celescope Catalog of Ultraviolet Stellar Observations* (Washington: Smithsonian Press).
Deharveng, J. M., Laget, M., Monnet, G., and Vuillemin, A. 1976, *Astr. Ap.*, **50**, 371.
Deutschman, W. A., Davis, R. J., and Schild, R. E. 1976, *Ap. J. Suppl.*, **30**, 97 (D).
de Vaucouleurs, G. 1958, *Ap. J.*, **128**, 465.
Hills, J. G. 1971, *Astr. Ap.*, **12**, 1.
Johnson, H. L. 1958, *Lowell Obs. Bull.*, **4**, 37.
———. 1965, *Ap. J.*, **141**, 923.
———. 1968, in *Nebulae and Interstellar Matter*, ed. B. Middlehurst and L. H. Aller (Chicago: University of Chicago Press), p. 167.
Johnson, H. L., and Morgan, W. W. 1953, *Ap. J.*, **117**, 313.
Jones, W. B., Obitts, D. L., Gallet, R. M., and de Vaucouleurs, G. 1967, Pub. Dept. of Astr. University of Texas at Austin, Ser. 2, Vol. **1**, No. 8.
Kurucz, R. L., Peytremann, E., and Avrett, E. H. 1974, *Blanketed Model Atmospheres for Early-Type Stars* (Washington: Smithsonian Press) (KPA).
Mathews, T. A., and Sandage, A. R. 1963, *Ap. J.*, **138**, 30.
Page, T. L., and Carruthers, G. R. 1977, in *COSPAR Space Research*, Vol. **17**, ed. M. J. Rycroft and A. C. Stickland (New York: Pergamon Press), p. 749.
Rose, W. K., and Tinsley, B. M. 1974, *Ap. J.*, **190**, 243.
Spinrad, H., Gunn, J. E., Taylor, B. J., McClure, R. D., and Young, J. W. 1971, *Ap. J.*, **164**, 11.
Tinsley, B. M. 1971, *Astr. Ap.*, **15**, 403.
———. 1972, in *Scientific Results from the Orbiting Astronomical Observatory* (*OAO-2*), ed. A. D. Code (NASA SP-310), p. 575.
Underhill, A. B. 1966, *The Early Type Stars* (Dordrecht: Reidel).

GEORGE R. CARRUTHERS and CHET B. OPAL: E. O. Hulburt Center for Space Research, Code 7123, Naval Research Laboratory, Washington, DC 20375

HARRY M. HECKATHORN: Department of Physics, Johns Hopkins University, Baltimore, MD 21218

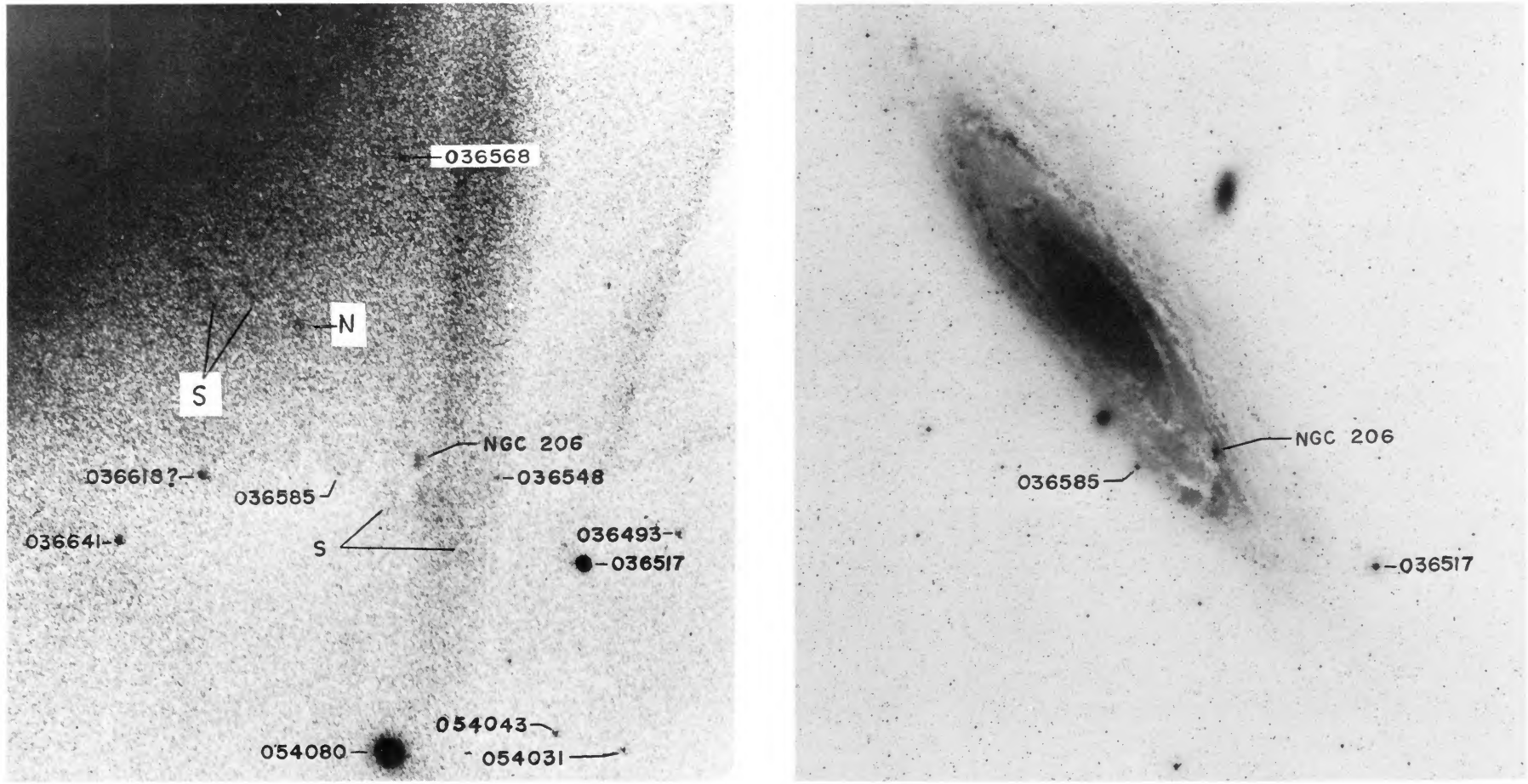

FIG. 1.—Negative print of a portion of the 101.6 s far-UV exposure of M31 compared with a ground-based (Palomar 48 inch Schmidt, Sky Survey plate 0-851) photograph in blue light. The two conspicuous UV sources are indicated as is the general spiral-arm structure which is faintly visible. The reproduction of the electrograph has been dodged during printing to reduce the compromising effect of corona discharge fogging.

CARRUTHERS *et al.* (*see* page 347)